JOURNAL OF SPACECRAFT AND ROCKETS
Vol. 44, No. 2, March–April 2007

Parametric Study of Deployment of Tethered Satellite Systems

Parag Mantri,* Andre P. Mazzoleni,† and David A. Padgett*
North Carolina State University, Raleigh, North Carolina 27695

DOI: 10.2514/1.22955

Deployment of a tethered satellite system is the process of separating the two end bodies by spooling out the tether connecting them. In this paper, we describe a 3-D model of a tethered satellite system undergoing deployment. From the equations of motion obtained using the 3-D model, we identify five system parameters that affect the length to which a tethered satellite system will deploy. The equations of motion describing the tether deployment are solved for a given range of each of the parameters to determine the effect of each of the parameters on the level of deployment reached. The equations are then nondimensionalized; nondimensionalization reduces the number of system parameters from five to two and increases the generality of the equations of motion. The nondimensional equations of motion are solved numerically, and the results are presented in charts and plots that can be used by mission designers to predict the final deployed length under given operating conditions. Two case studies are presented to demonstrate the utility of these tools.

Nomenclature

G = universal gravitational constant, $6.6742 \times 10^{-11}\ \mathrm{m}^3/\mathrm{s}^2 \cdot \mathrm{kg}$
g = gravitational acceleration at the surface of the Earth, $9.8\ \mathrm{m/s}^2$
h = orbital altitude
L = deployed length of the tether
$\tilde{L}$ = nondimensional tether length, L/L_f
L_f = total length of the tether
$\tilde{L}_0'$ = nondimensional initial separation velocity, $\dot{L}(0)/(\Omega L_f)$
M_e = mass of the Earth, 5.98×10^{24} kg
$\bar{m}$ = effective mass, $m_A m_B/(m_A + m_B)$
m_A, m_B = two end bodies of the satellite
R_e = radius of the Earth, 6378 km
R_0 = orbital radius, $R_e + h$
T_0 = tether tension
$\tilde{T}_0$ = nondimensional tether tension, $T_0/(\bar{m} L_f \Omega^2)$
$\tilde{t}$ = nondimensional time, $t\Omega$
θ = "pitch" angle, the in-plane angle between tether axis and the local vertical
ϕ = "roll" angle, the out-of-plane angle between tether axis and the local vertical
Ω = orbital angular velocity, $\Omega^2 = GM_e/(R_e + h)^3$

Superscripts

$'$ = first derivative with respect to nondimensional time
$''$ = second derivative with respect to nondimensional time

I. Introduction

SPACE tethers are long members that connect two or more end bodies in the space environment. The tether tension force acting on the end bodies influences the dynamics of the entire system. Because of the variety of interesting dynamics they exhibit, space tethers have many scientific and research applications [1,2]. Some space tether applications are rudimentary; for example, space tethers are used to ensure that astronauts and equipment do not separate from a vehicle during space walks [3]. More sophisticated applications of space tethers are presented next.

Electrodynamic tethers reduce the need for conventional energy sources such as chemical propellants and even stored electrical power [2,4]. As a conductive tether travels with high velocity through the Earth's magnetic field, a Lorentz force can be imparted to the tether by forcing current through the tether; this force can be used for orbital transfer [5]. In addition to providing orbital propulsion, electrodynamic tethers can be used to deorbit low-Earth-orbit (LEO) satellites that have fulfilled their missions; such satellites would be designed to deploy an electrodynamic tether to initiate the deorbiting process. After the satellite is deorbited in a controlled manner, it no longer poses a collision threat to other satellites in LEO [6–8]. Beyond simply enhancing the capabilities of satellite systems, tethers have also attracted considerable interest among researchers as data-gathering and space access tools; a number of these applications have been proposed [9–12]. One such tethered system concept under study uses tethered satellites to employ a momentum transfer technique with the goal of transferring payloads from low orbit to a higher orbit [13,14]. One far-term application of space tethers is a "space elevator" [13,15,16]. Space elevators consist of a cable that is deployed by a satellite in geosynchronous orbit. The purpose of a space elevator is to provide support for crawlers that move from the surface of the earth to space; space elevators present an economical alternative to chemical rockets for delivering payloads to space. Tethered satellites can also be used to produce an artificial gravity effect in orbit. The artificial gravity effect produced by a rotating body is currently under study because significant bone and muscle loss can occur in humans exposed to a microgravity environment for long periods of time [17]. The tethered artificial gravity (TAG) satellite mission was designed to study the operation and dynamics of an artificial-gravity-generating tethered satellite system. The TAG mission profile involves boosting the TAG system to LEO in a packaged configuration using a conventional rocket, deploying the tether, and then causing the system to spin about its center of mass to produce an artificial gravitational effect on bodies located within the end bodies. Preliminary studies of the TAG system deployment dynamics have been performed assuming nearly equal end-body masses [17]. A detailed list of other applications of space tethers and tethered satellites can be found in the Tethers in Space Handbook [18].

Many tethered satellite missions, including the ones discussed in the preceding paragraphs, have mission profiles that involve a packaged body being launched into orbit and deployed. These missions generally require that the tether deploys completely for the

---

Received 3 February 2006; revision received 1 January 2007; accepted for publication 9 January 2007. Copyright © 2007 by Andre P. Mazzoleni. Published by the American Institute of Aeronautics and Astronautics, Inc., with permission. Copies of this paper may be made for personal or internal use, on condition that the copier pay the $10.00 per-copy fee to the Copyright Clearance Center, Inc., 222 Rosewood Drive, Danvers, MA 01923; include the code 0022-4650/07 $10.00 in correspondence with the CCC.

*Graduate Research Assistant, Department of Mechanical and Aerospace Engineering. Member AIAA.

†Associate Professor, Department of Mechanical and Aerospace Engineering. Associate Fellow AIAA.

mission to be successful. Lack of full deployment can endanger the craft, any crew members that are present, and result in behavior outside the operational envelope for most systems; such behavior is to be avoided. To ensure the success of future missions requiring tether deployment, it is necessary to study the factors that affect tether deployment. In this paper, we will examine the general tethered satellite equations of motion to identify the factors that affect tether deployment, and we will perform a parametric analysis of the parameters present in the equations of motion to determine the effect of each identified parameter on the final deployed length achieved. In the course of this study, we will identify trends and tendencies of the system deployment with respect to the identified system parameters and develop tools capable of qualitatively and quantitatively predicting the final deployed length achieved for a given set of parameters. These tools will be of assistance to mission planners in that they will clearly delineate the combinations of parameters that result in full tethered system deployment.

The literature is rich with papers detailing analytical and numerical studies of the equations of motion of tethered satellite systems with the goal of evaluating or determining control laws [19–21]. The goal of this paper, however, is to numerically examine the dynamics of a deploying tethered satellite system in an uncontrolled state. Such a system is analogous to that employed by the small expendable deployer system (SEDS) missions flown in the early 1990s [22,23]. We accomplish this goal by numerically integrating the equations of motion of the system and adjusting the initial conditions of the system to simulate a deploying system. Such deploying systems have been studied by Grassi and Cosmo [24] and Mazzoleni [25], who both examined the effect of initial alignment on end-body attitude stability and the importance of initial alignment to overall deployment performance. We expand on these works by varying five different parameters that affect the dynamics of the tethered satellite system. We determine the effect of each of these parameters individually and then, through nondimensionalization, show that the dynamics of the tethered satellite system are determined through equations of motion governed by two nondimensional parameters. We determine the behavior of the system under a variety of different combinations of these two parameters.

II. Model

The system used as a prototypical tethered satellite in this paper is similar to that of the TAG satellite mission discussed in the preceding section and described in detail by Mazzoleni and Hoffman [17]. A simplified model of the system consists of two point masses connected by a massless tether. The center of mass of the system is assumed to move in a circular orbit about the Earth; the result of this assumption is that the orbital height h and the orbital angular frequency Ω are both constant [26]. The tether is considered to be a rigid, inextensible rod that is capable of nonelastic changes in length through a spooling-out process. We have shown previously that the rigid-rod model (also known as a planar dumbbell model) can be a good approximation to the behavior of a real tethered system . We also assume that the spool inertia is negligible, the length of the tether is small compared to the distance between the center of the Earth and the center of mass of the tethered satellite system, and that gravity and the tether tension force are the only forces that act on the end bodies of the tethered satellite system. For the purposes of this paper, the total mass of the satellite (the sum of the two end-body masses) is assumed to be 70 kg and the mass of the tether is assumed to be negligible. We also assume that the deployer friction remains constant throughout the deployment process and that the tension force traveling through the tether is equal to the deployer friction. The assumption that the deployer friction (and thus the tether tension) remains constant throughout the spooling process represents a simplified approximation of actual deployer friction profiles and was made to keep the analysis as general as possible. Whereas most deployer friction profiles vary with parameters such as the deployment velocity, simulations performed assuming constant deployer friction can represent worst-case scenarios or can give insight into deployment characteristics under average deployer friction conditions. The initial velocity that separates the two end bodies to begin the spooling-out process is assumed to be imparted by a spring mounted in one of the two end bodies [25]. The deployment is unforced beyond the action of the spring and hence not controlled by any external system. The motion of the satellite is defined so that at any point in time, the in-plane angle θ and the out-of-plane angle ϕ fall in the range −90 to 90 deg. These angles are defined with respect to the local vertical ($\theta = 0$) and the orbital plane ($\phi = 0$). Under this definition, $\theta = \phi = 0$ is the position where the tether axis is aligned to the local vertical and is completely in the orbital plane. As the tether spools out and increases in length, the satellite rotates in and out of the orbital plane. The spool-out process eventually stops after deploying to some length and the remainder of the mission can be initiated. In this paper, the dynamics occurring after the spool-out process is complete are ignored; this paper is concerned only with the deployment process. Sketches of the stages involved in deployment and the angles θ and ϕ are shown in Figs. 1 and 2, respectively.

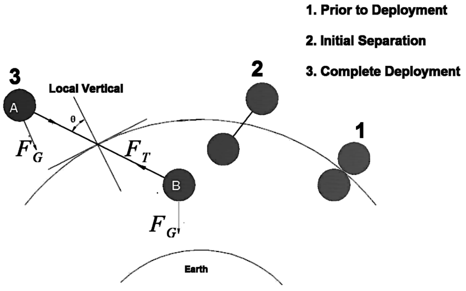

Fig. 1 Deployment steps, adapted from the *Tethers in Space Handbook* [18].

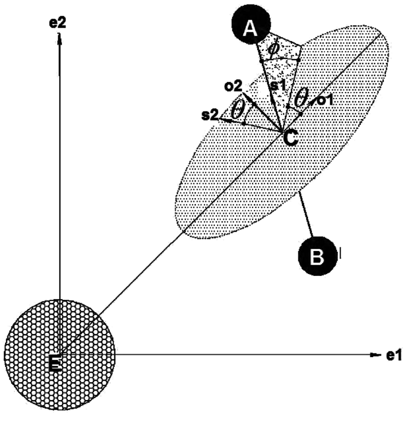

Fig. 2 Representation of θ and ϕ.

III. Equations of Motion

The derivation of the equations of motion was carried out using Newton's Second Law. The derivation confirms the standard nonplanar equations of motion for a tethered satellite system as presented by Mazzoleni [25] and as derived in the appendix to this paper; these equations are

$$\ddot{L} = L[(\dot{\theta} + \Omega)^2\cos^2\phi + \dot{\phi}^2 + 3\Omega^2\cos^2\theta\cos^2\phi - \Omega^2] - \frac{T}{\bar{m}} \quad (1)$$

$$\ddot{\theta} = 2(\dot{\theta} + \Omega)\dot{\phi}\tan\phi - 2\frac{\dot{L}}{L}(\dot{\theta} + \Omega) - 3\Omega^2\cos\theta\sin\theta \quad (2)$$

$$\ddot{\phi} = -2\frac{\dot{L}}{L}\dot{\phi} - [(\dot{\theta} + \Omega)^2 + 3\Omega^2\cos^2\theta]\cos\phi\sin\phi \quad (3)$$

The quantities L, θ, and ϕ are three time-dependent variables, which are determined under appropriate initial conditions. For the purposes of simulation, we assume that the system starts from rest with respect to the orbital reference frame $[\dot{\theta}(0) = \dot{\phi}(0) = 0]$. Also, because the tether is completely wound in one of the end bodies, the initial tether length before deployment, $L(0)$, is also zero. However, to avoid mathematical error during numerical simulation [due to the term L/L in Eq. (3)], we approximate $L(0)$ to be a very small number; in practice, we make the approximation $L(0) \approx 10^{-5}$. The angular alignment of the system with respect to the orbital plane before the start of deployment is specified by $\theta(0)$ and $\phi(0)$ and is referred to as the initial position (IP) of the system. Because one of the objectives of this paper is to understand the deployment performance as a function of the system IP, we use combinations of $\theta(0)$ and $\phi(0)$ spanning from −90 to 90 deg in steps of 5 deg, that is, a total of 1369 IPs for each simulation. To solve these equations, we need to specify the tether tension T_0 , the initial separation velocity $\dot{L}_0$, the system effective mass $\bar{m}$, the total tether length L_f, and the orbital angular velocity of center of mass Ω. These quantities are the five parameters that completely describe the dynamics of the tethered system for a given IP and they must be specified for every mission. Note that the initial separation velocity (the separation velocity at instant $t = 0$) does not appear explicitly in the equations of motion but must be specified as an initial condition when solving these equations. When designing a mission, it is likely that the orbital altitude of the tethered satellite will be of more importance than the orbital angular velocity. However, note that the orbital angular velocity is a function only of constant parameters and the orbital altitude $[\Omega^2 = GM_e/(R_e + h)^3]$. Therefore, we replace Ω by orbital altitude h in the list of parameters that affect tethered satellite motion. The five parameters discussed are collectively referred to as *system parameters*. Once these system parameters are specified, the system dynamics can be simulated. Each simulation is repeated over the entire range of IP (1369 values). Each case is simulated until either the separation velocity reaches zero or until the deployed length reaches the total tether length (i.e., $\dot{L} = 0$ or $L = L_f$). Because, for the deployer systems considered for this study, static friction is assumed to be significantly higher than the kinetic friction, we assume that there will not be any deployment after the deployment speed reaches zero, justifying the condition $\dot{L} = 0$ for simulation termination.

IV. Operating Ranges of Dimensional Parameters

Among the system parameters, T_0, $\bar{m}$, and $\dot{L}_0$ are functions of the system design and hence are collectively referred to as *design parameters*. The remaining two parameters, h and L_f, are requirements for each mission irrespective of deployment performance that can be achieved, and hence they would be collectively referred to as *mission parameters*. Under these definitions, a mission with $T_0 = 100$ mN, $\bar{m} = 15$ kg, and $\dot{L}_0 = 5$ m/s, $h = 1000$ km and $L_f = 5$ km would be denoted as a mission with design parameters [$T_0 = 100$ mN, $\bar{m} = 5$ kg, $\dot{L}_0 = 5$ m/s] and mission parameters [$h = 100$ km, $L_f = 5$ km]. Note that the tension is expressed in mN, separation velocity in m/s, and orbital altitude and tether length in km. From the design perspective, we have more liberty to change design parameters than the mission parameters; therefore the following section will detail deployment performance as a function of the design parameters. As for the mission parameters, we work in the range 100–10,000 m for total tether length L_f and 300–1200 km for orbital altitude h. These ranges are selected on the basis of typical values of these parameters for similar missions. The operating ranges of design parameters for this analysis is determined from information detailed by Mazzoleni [28]:

1) Tether tension/deployer friction T_0: When the tether is being spooled out, the friction between the tether and the deployer accounts for the tether tension. As long as the tether is being deployed, the tether tension is equal to the deployer friction. However, after tether deployment is complete, there is no deployer friction but it is possible that the tethered system is rotating with respect to the orbital reference frame. The centripetal acceleration that allows the end bodies to rotate around each other without moving away from each other is provided by a tension traveling through the tether; that is, after deployment the tether tension can be nonzero despite the fact that the deployer friction force is zero [29,30]. However, this paper concentrates only on the tether deployment process, and thus the tether tension force is assumed to be equal to the tether deployer friction force for all simulations. We also assume that the tether tension remains constant throughout the deployment process. This is not always true especially in systems with high ejection velocity. However, as is discussed in the next paragraph, for the purposes of this paper we do not consider very high ejection velocities. Experiments on proposed tether deployers have shown that tether tension due to deployer friction is of the order 50 mN at room temperature [25]. However, because the effects of extreme temperatures and other conditions in orbit are not known, we use a safety factor of 4 and assume that the deployer friction can take values as high as 200 mN. Hence, the operating range of tether tension T_0 is [50 mN, 200 mN].

2) Initial separation velocity $\dot{L}_0$: The initial separation velocity is imparted by the springs mounted on the deployer, and hence it is directly dependent on the spring constant and degree of compression of the springs. Based on a previous study performed by Mazzoleni [25], the operating range for this parameter is selected to be [3 m/s, 6 m/s]. Because of space limitations on the deployer, the maximum spring size and spring compression are both limited; therefore, the maximum deployment velocity is limited. We assume that this maximum velocity is 6 m/s.

3) Effective mass $\bar{m}$: The effective mass is defined as $\bar{m} = m_A m_B/(m_A + m_B)$. The dynamics of a tethered satellite are more closely related to the mass distribution between the tethered satellite end bodies than to the total mass of the tethered satellite. For this reason, the total end-body mass of 70 kg is constant throughout the paper and the distribution of this mass on either end is varied. The value of $\bar{m}$ is at a maximum when the masses are equally distributed and is at a minimum when the difference between the mass of the two end bodies is greatest, that is, when one of the end bodies has the minimum allowed mass. To accommodate the hardware and instruments, the mass of each end body must have a lower bound; that lower bound is assumed to be 12 kg for this study. Therefore, the range of $\bar{m}$ for a 70-kg total mass can be shown to be [10 kg, 17.5 kg].

Having defined the operating range of each of the parameters, we can now determine the solutions to the equations of motion. For each set of system parameters, the total deployed length is plotted as a function of its IP on 2-D and 3-D plots as shown in Figs. 3–11. We also compute the average of all the final deployed lengths achieved at each IP, [referred to as average deployment (AD)] and the percentage of the IPs resulting in full deployment, [referred to as percentage of full deployment (PFD) in this paper]. Note that the terms “full deployment” or “complete deployment” are used to indicate situations when for a given IP, the final deployed length is at least equal to the total tether length $L = L_f$. The term “level of deployment” is used to represent the percentage of total tether length to which the tether is deployed.

The AD of a tethered system measures the probability of a successful deployment (and thus a successful mission) and hence it is of interest because there conceivably are missions that can be completed with a high degree of success even if a tethered satellite system achieves a high (but not necessarily full) level of deployment. An AD of 100% indicates that all the IPs have deployed completely, whereas an AD of 0% indicates that none of the IPs have deployed at all. Similarly, 100% PFD indicates all the IPs have deployed completely (effectively same as 100% AD) and 0% PFD indicates that none of the IPs have reached complete deployment (note that this is not equivalent to 0% AD).

Both the 2-D and 3-D plots are generated from the same data. However, they may not necessarily give redundant information. The 3-D plots are generated from calculations of the deployment achieved at each IP and hence the level of deployment for each of the simulated IPs can be determined. However, it can sometimes be difficult to read the deployment level from the 3-D plots. Therefore, to present the data in a more readable form, the range of deployment, that is, 0–100% of total tether length deployed, is divided into six intervals and each interval is assigned to a shade of gray from black to white. A grid is generated on the θ–ϕ plane such that each element of the grid corresponds to a unique IP. Then, each point on the plane is colored with a shade of gray based on the deployment performance of the IPs. The shades of gray act as third axis and present the deployment performance on a 2-D plot instead of a 3-D plot. Although these plots do not give precise deployment achieved at a given IP, they are more effective than 3-D plots in determining the deployment of any given IP within 25%.

We now examine the effect of each of the design parameters [T_0, $\bar{m}$, $\dot{L}_0$] on deployment performance. For this entire analysis, we select mission parameters [$h = 1200$ km, $L_f = 2.85$ km]. Each of the design parameters is varied one at a time within their operating range. Note that the numerical method used to generate all simulations discussed in this paper is the MATLAB® ode45 method; this method is a Dormand–Prince pair that uses a fourth-order Runge–Kutta scheme with an adaptive time step. The scheme is fourth-order accurate with respect to the time step.

A. Effect of Effective Mass $\bar{m}$ (Figs. 3–5)

For Figs. 3–5, T_0 is 100 mN and $\dot{L}_0$ is 5 m/s. We vary $\bar{m}$ from its minimum value of 10 kg to its maximum value of 17.5 kg. We start with $\bar{m} = 10$ kg, the results of which are presented in Fig. 3; the design parameters for this case are [$T_0 = 100$ mN, $\bar{m} = 10$ kg, $\dot{L}_0 = 5$ m/s]. Upon inspection of both Figs. 3a and 3b, we see that the deployment is fairly uniform for all of the IPs except for a small portion at the center of each plot, which shows a slightly higher level of deployment. The AD is below 50% and the PFD is 0%. In Fig. 3b, we see that the small portion in the center of the plot (indicating a higher level of deployment), is in the [50, 75)% range and the rest of the plot has a uniform shade representing [25, 50)% AD. The absence of a white region in this plot shows that none of the IPs result in full deployment; thus the PFD is 0%. In Fig. 4, the effective mass is raised to 15 kg and we see a prominent increase in the AD of the system to about 66%. However, less than 1% of IPs result in full deployment as indicated by the PFD of about 0.5%. This small fraction of IPs resulting in complete deployment can be seen in Fig. 4b as a small white region at the center of the plot. This white region is surrounded by another small region of [75, 100)% deployment and the rest of the plot has a shade representing [50, 75)% AD. Finally, for Fig. 5, we increase $\bar{m}$ to its maximum value of 17.5 kg. We can see that the AD is slightly above 75% and the PFD also increases considerably to about 16%. Figure 5b has same three shades of gray as in Fig. 4b, but the white region representing the full deployment in Fig. 5b is bigger than the corresponding white region in Fig. 4b. Clearly, the level of deployment has increased as we progress from Figs. 3–5, which indicates that the deployment favors higher effective mass; therefore, to achieve full deployment, the end-body masses should be distributed as uniformly as possible.

B. Effect of Tether Tension T_0 (Figs. 6 and 7)

For Figs. 6 and 7, $\bar{m}$ is 17.5 kg and $\dot{L}_0$ is 4 m/s. We vary T_0 from 100 mN to its minimum value of 50 mN. The design parameters for Fig. 6a are [$T_0 = 100$ mN, $\bar{m} = 17.5$ kg, $\dot{L}_0 = 4$ m/s]. We can see that the AD is slightly below 50% whereas the PFD is 0%. In Fig. 6b we see a region of [50, 75)% deployment level develop in the center

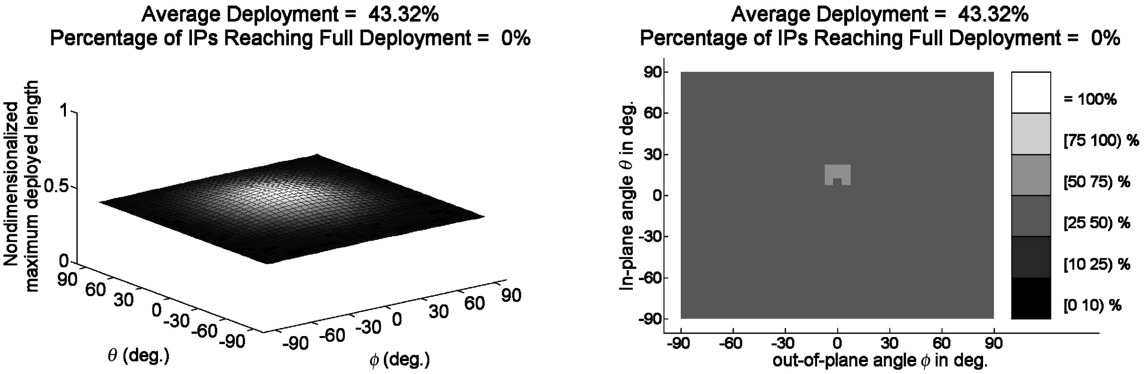

a) 3-D representation with IPs on horizontal plane and deployed length on vertical axis

b) 2-D representation with ϕ on horizontal axis and θ on vertical axis

Fig. 3 Deployment as a function of IPs at [$T_0 = 100$ mN, $\bar{m} = 10$ kg, $\dot{L}_0 = 5$ m/s].

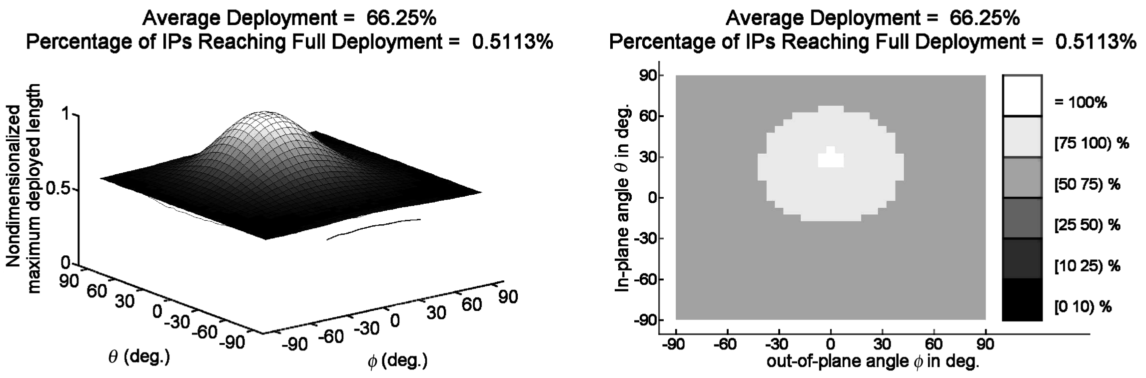

a) 3-D representation with IPs on horizontal plane and deployed length on vertical axis

b) 2-D representation with ϕ on horizontal axis and θ on vertical axis

Fig. 4 Deployment as a function of IPs at [$T_0 = 100$ mN, $\bar{m} = 15$ kg, $\dot{L}_0 = 5$ m/s].

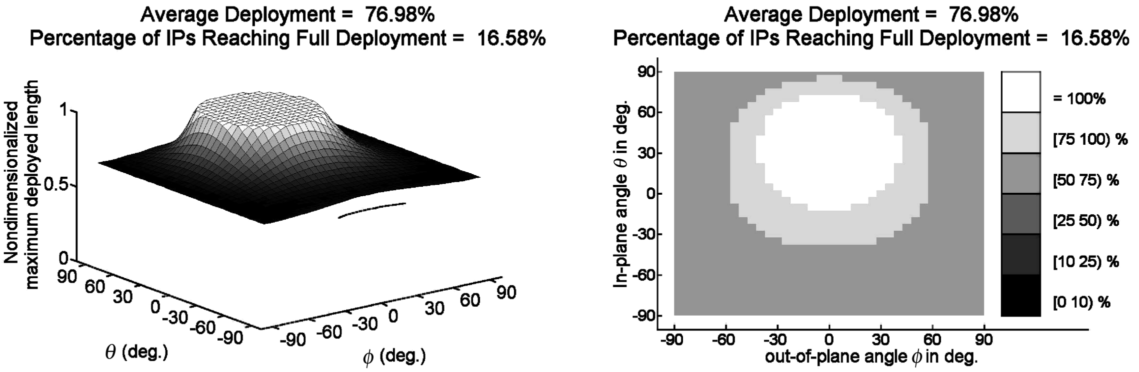

a) 3-D representation with IPs on horizontal plane and deployed length on vertical axis

b) 2-D representation with ϕ on horizontal axis and θ on vertical axis

Fig. 5 **Deployment as a function of IPs at $[T_0 = 100\ \mathrm{mN}, \bar{m} = 17.5\ \mathrm{kg}, \dot{L}_0 = 5\ \mathrm{m/s}]$.**

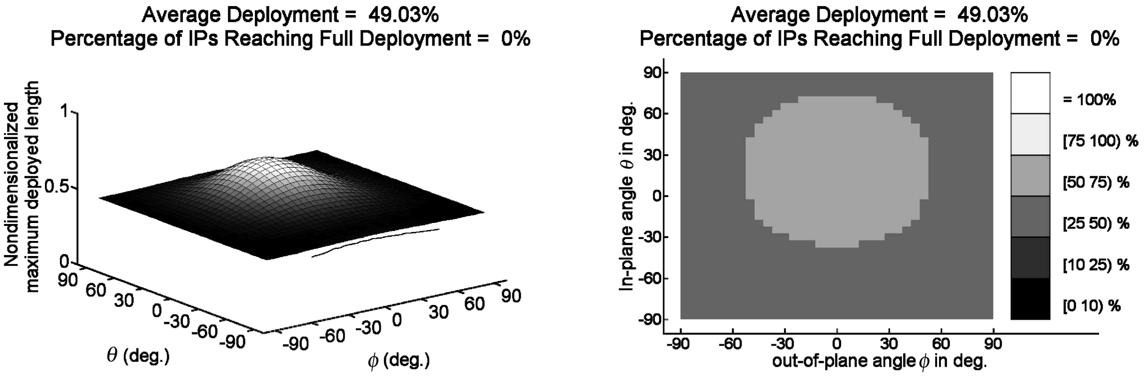

a) 3-D representation with IPs on horizontal plane and deployed length on vertical axis

b) 2-D representation with ϕ on horizontal axis and θ on vertical axis

Fig. 6 **Deployment as a function of IPs at $[T_0 = 100\ \mathrm{mN}, \bar{m} = 17.5\ \mathrm{kg}, \dot{L}_0 = 4\ \mathrm{m/s}]$.**

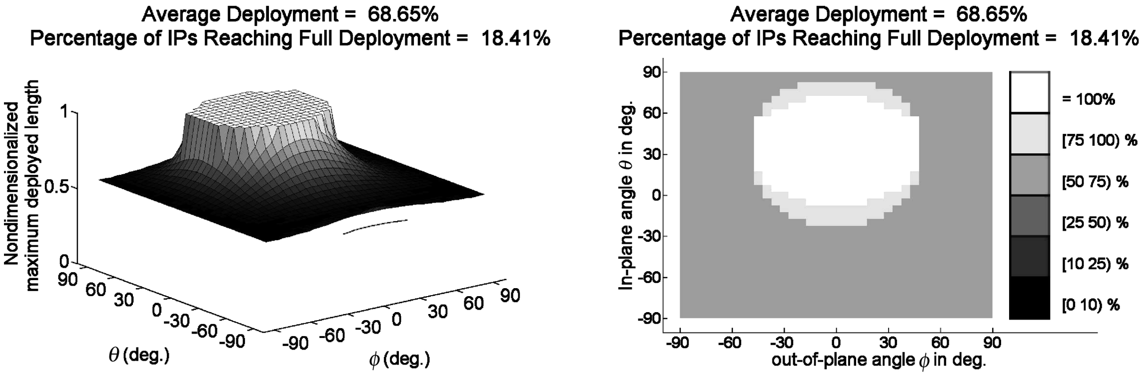

a) 3-D representation with IPs on horizontal plane and deployed length on vertical axis

b) 2-D representation with ϕ on horizontal axis and θ on vertical axis

Fig. 7 **Deployment as a function of IPs at $[T_0 = 75\ \mathrm{mN}, \bar{m} = 17.5\ \mathrm{kg}, \dot{L}_0 = 4\ \mathrm{m/s}]$.**

of the plot surrounded by a region of [25, 50)% in the rest of the plot. There is still no white region anywhere on the plot and the calculated PFD is 0%. For Fig. 8, the tether tension is reduced to 75 mN. We see that the AD increases to about 68% and about 18% of IPs result in full deployment. This fraction of PFD can be seen in Fig. 8b as a white region at the center of the plot. This white region is surrounded by a region of [75, 100)% of full deployment and the rest of the plot has a shade representing [50, 75)% deployment. Finally, in Fig. 7, where T_0 is at its minimum value of 50 mN, we calculate that the AD has increased to about 88% and the PFD has increased to about 48%. Again, Fig. 7b has the same three shades of gray as in Fig. 8b, but the region of full deployment and region of [75, 100)% deployment have both spread out widely, touching the top edge of the plot and reemerging from the bottom. These plots indicate that with decreasing deployer friction the total level of deployment reached by a tethered satellite system increases. This conclusion is consistent with the fact that friction opposes motion in general and, specifically, deployer friction opposes tether deployment.

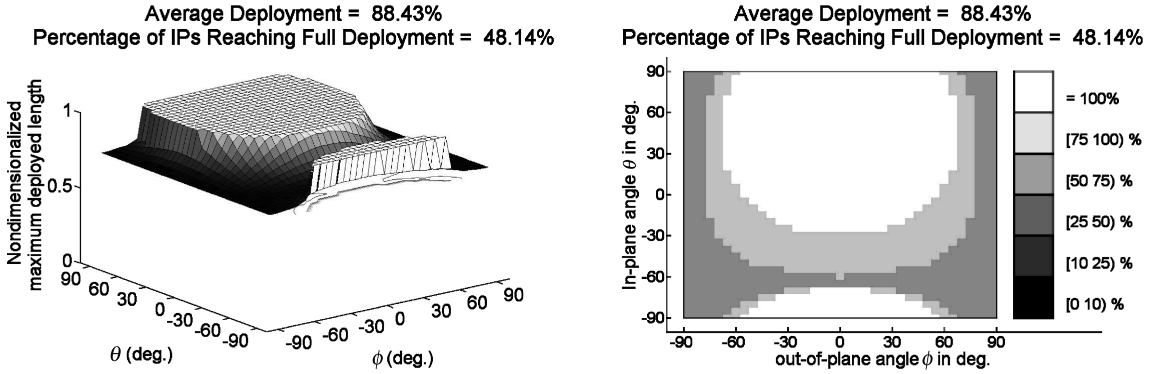
Average Deployment = 88.43%
Percentage of IPs Reaching Full Deployment = 48.14%

a) 3-D representation with IPs on horizontal plane and deployed length on vertical axis

b) 2-D representation with ϕ on horizontal axis and θ on vertical axis

Fig. 8 Deployment as a function of IC at [$T_0 = 50$ mN, $\bar{m} = 17.5$ kg, $\dot{L}_0 = 4$ m/s].

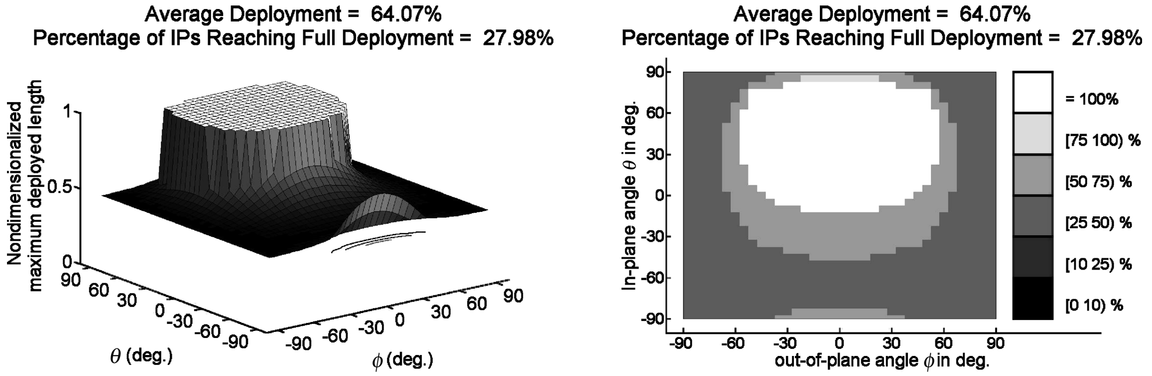
Average Deployment = 64.07%
Percentage of IPs Reaching Full Deployment = 27.98%

a) 3-D representation with IPs on horizontal plane and deployed length on vertical axis

b) 2-D representation with ϕ on horizontal axis and θ on vertical axis

Fig. 9 Deployment as a function of IPs at [$T_0 = 50$ mN, $\bar{m} = 17.5$ kg, $\dot{L}_0 = 3$ m/s].

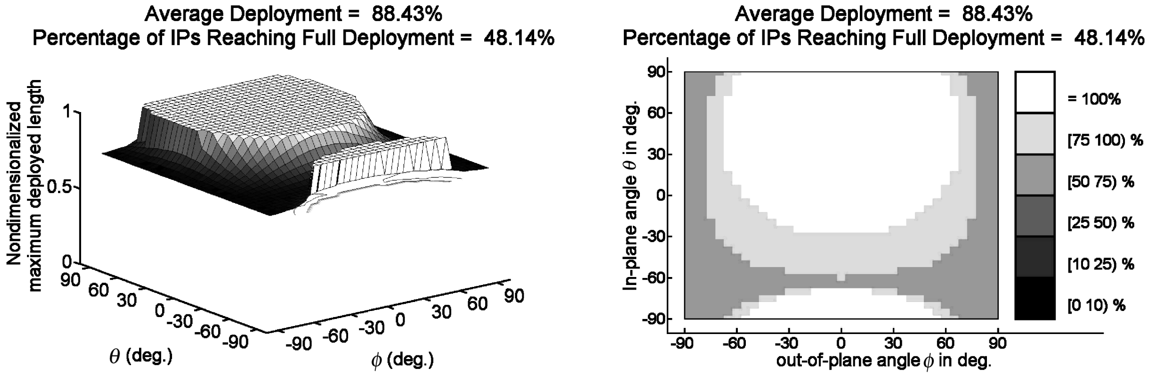
Average Deployment = 88.43%
Percentage of IPs Reaching Full Deployment = 48.14%

a) 3-D representation with IPs on horizontal plane and deployed length on vertical axis

b) 2-D representation with ϕ on horizontal axis and θ on vertical axis

Fig. 10 Deployment as a function of IPs at [$T_0 = 50$ mN, $\bar{m} = 17.5$ kg, $\dot{L}_0 = 4$ m/s].

C. Effect of Initial Separation Velocity $\dot{L}_0$ (Figs. 9–11)

For Figs. 9–11, $\bar{m}$ has a value of 17.5 kg (the maximum value of $\bar{m}$ considered in this paper) and T_0 has a value of 50 mN (the minimum value of T_0 considered in this paper). From the preceding two sections, we can conclude that these two parameters are optimized for full deployment. To determine the effect of the initial separation velocity on AD and PFD, we vary $\dot{L}_0$ from 3 to 5 m/s. We can see that for this configuration of [$T_0 = 50$ mN, $\bar{m} = 17.5$ kg, $\dot{L}_0 = 3$ m/s] (illustrated by Fig. 9), the AD is about 64% whereas the PFD is about 28%. Figure 9b shows that the region of high deployment on the 2-D shaded plot spreads outward from the center of the plot; this is consistent with previous 2-D shaded plots. Note that the shaded plots seem to be periodic in nature respect to the in-plane angle θ; that is, if the top of a shade plot is folded down to meet the bottom of the shade plot, the shaded regions match. The matching of the shading regions at the top and the bottom of the shaded plots

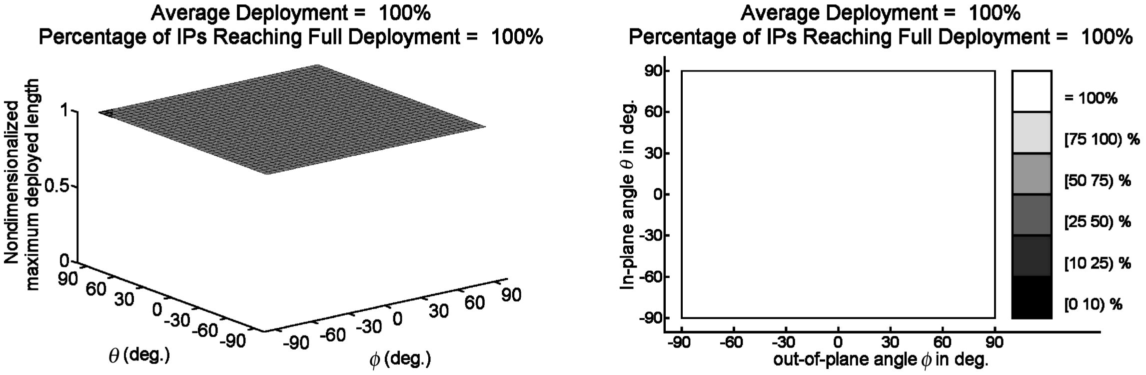

a) 3-D representation with IPs on horizontal plane and deployed length on vertical axis

b) 2-D representation with ϕ on horizontal axis and θ on vertical axis

Fig. 11 Deployment as a function of IPs at [$T_0 = 50$ mN, $\bar{m} = 17.5$ kg, $\dot{L}_0 = 5$ m/s].

indicate a symmetry of the tethered satellite configuration with respect to the in-plane angle θ. We see the corresponding behavior in 3-D representation in Fig. 9a. For Fig. 10, we increase the initial separation velocity to 4 m/s. We calculate that the AD has increased to about 88% and about 48% of IPs result in full deployment. Note that this configuration is identical to one studied in the preceding subsection for Fig. 7. Finally for Fig. 11, we increase the separation velocity to 5 m/s. We can see that the AD is now 100%, which indicates that PFD is also 100%. This is the ideal deployment scenario because each simulated IP results in full deployment. In Fig. 11b we see that the entire plot is white, which indicates complete deployment of all of the simulated IPs. Note that the deployment has increased with increases in $\dot{L}_0$ and this is consistent with the intuitive expectation that higher initial separation velocities should result in a higher probability of deployment. We have shown that full tethered satellite deployment can be achieved when the initial separation velocity is 5 m/s. Recall that in the definition of the operating ranges for each variable, we indicated that the operating range of the initial separation velocity is [3 m/s, 6 m/s]. Because complete deployment can be achieved at an initial separation velocity of 5 m/s, we assume that full deployment is achieved for any initial separation velocity greater than 5 m/s; this indicates that the effective operating range for which useful data may be gathered is [3 m/s, 5 m/s]. Therefore, simulations using larger separation velocities than 5 m/s are not presented in this paper. The trends of both the AD and the PFD as a function of tether tension, effective mass, and initial deployment velocity are shown in Table 1.

A general observation concerning the previously described simulations is that for IPs closer to $\theta = 0$ and $\phi = 0$, that is, the IPs located at the center of the 2-D shaded plot, a high level of deployment is reached for a wider range of tethered satellite configurations than simulations involving IPs near the edge of the 2-D plots. In other words, if the design parameters do not result in complete deployment for all simulated IPs, the IPs that are closer to $[\theta(0), \phi(0)] = (0, 0)$ tend to deploy to a higher level than those far from the point $[\theta(0), \phi(0)] = (0, 0)$. This suggests that before deployment, the system should be initially aligned close to the local vertical and in the orbital plane. Note that the region of high deployment tends to spread symmetrically about the line $\phi = 0$ as the design parameters result in higher levels of deployment. However, the region of high deployment does not spread symmetrically about the line $\theta = 0$. In other words, the deployment plots are symmetrical about the $\phi(0)$ axis but not about the $\theta(0)$ axis. Note also that the regions of high deployment are larger on the half of the IP plane that contains positive $\theta(0)$ values; this indicates that the deployment occurs more readily for positive initial in-plane angles than for negative initial in-plane angles. This asymmetry may be due to the interaction between the gravity gradient torque and the orbital angular velocity of the system; this hypothesis is a subject for further mathematical investigation. However, upon inspection of the equations of motion [Eqs. (1–3)], it can be seen that the equations are symmetric with respect to ϕ but not with respect to θ, which is consistent with the observations regarding the deployment plots.

Table 1 Deployment results as a function of increasing or decreasing individual dimensional parameters

T_0, mN	$\bar{m}$, kg	$\dot{L}_0$, m/s	Average deployment, %	IPs reaching complete deployment, %
100	**10**	5.0	43.32	0
100	**15**	5.0	66.25	0.51
100	**17.5**	5.0	76.98	16.58
100	17.5	4	49.03	0
75	17.5	4	68.65	18.41
50	17.5	4	88.43	48.14
50	17.5	**3**	64.07	27.98
50	17.5	**4**	88.43	48.14
50	17.5	**5**	100	100

V. Nondimensionalization

Whereas the preceding analysis gives an overview of how each of the design parameters affects the deployment achieved by a given tethered satellite system, it has a few limitations:

1) Because each design parameter was varied only twice, we know the general trend of the deployment with respect to a given parameter, but we do not know at what point the level of deployment transitions from one range of deployment to another.

2) Because only one parameter at a time was varied, we do not know the effect of varying more than one (or even all) of the parameters at a time.

3) The analysis only examined the effect of the design parameters. The effect of varying mission parameters $[h, L_f]$ on the deployment performance was not evaluated.

To completely analyze the system, we study the effect of all the five system parameters $[T_0, \bar{m}, \dot{L}_0, h, L_f]$ and use multiple values of each parameter within their respective operating ranges and vary them simultaneously in different combinations. To reduce the complexity of this analysis, we nondimensionalize the equations of motion and thus reduce to two the number of parameters affecting the deployment.

We nondimensionalize the equations of motion by first introducing nondimensional basic units, nondimensional time $\tilde{t} = t\Omega$ and nondimensional length $\tilde{L} = L/L_f$. Then, using these nondimensional variables, we rewrite the equations of motion as

$$\tilde{L}'' = \tilde{L}[(\theta' + 1)^2\cos^2\phi + \phi'^2 + 3\cos^2\theta\cos^2\phi - 1] - \tilde{T}_0 \qquad (4)$$

$$\theta'' = 2(\theta' + 1)\phi' \tan\phi - 2\frac{\tilde{L}'}{\tilde{L}}(\theta' + 1) - 3\cos\theta\sin\theta \qquad (5)$$

$$\phi'' = -2\frac{\tilde{L}'}{\tilde{L}}\phi' - [(\theta' + 1)^2 + 3\cos^2\phi]\cos\phi\sin\phi \tag{6}$$

Note that all nondimensional variables are denoted by a top-placed tilde. Because θ and ϕ are nondimensional by definition, we drop the use of tildes on θ and ϕ. Also note that the superscript $'$ denotes the derivative of a given variable with respect to nondimensional time $\tilde{t}$ and not with respect to dimensional time.

In the preceding nondimensional equations of motion, the following two nondimensional parameters are introduced:

$$\tilde{T}_0 = \frac{T_0}{\tilde{m}L_f\Omega^2} \quad \text{and} \quad \tilde{L}'_0 = \frac{\dot{L}_0}{\Omega L_f} \tag{7}$$

Note that the definitions of these two nondimensional parameters include all of the design parameters $[T_0, \tilde{m}, \dot{L}_0]$ and mission parameters $[h, L_f]$ (h is included implicitly in Ω). In other words, variations of each of the five dimensional system parameters can be effectively reduced to variations of the two nondimensional parameters. Note that we no longer differentiate between design and mission parameters. Now we investigate the operating range of the nondimensional parameters based on the operating range of the corresponding dimensional system parameters. Based on the definitions of these two nondimensional parameters $\tilde{T}_0$ and $\tilde{L}'_0$ in Eq. (7), and using the ranges of each of the dimensional parameters discussed earlier, we can derive the range of $\tilde{T}_0$ as [0.21343, 218.31] and $\tilde{L}'_0$ as [0.25929, 62.87].

Even though the maximum value for $\tilde{L}'_0$ is calculated as 62.87, for values of $\tilde{L}'_0$ greater than 22, AD = PFD = 100% for any given value of $\tilde{T}_0$ within the range calculated earlier in this paper. Therefore, values of $\tilde{L}'_0$ beyond 22 are not investigated in this paper. For convenience, the range of $\tilde{T}_0$ is taken to be [0.1, 220] and the range of $\tilde{L}'_0$ is taken to be [0.2, 22]. Note that the analysis set forth in the remainder of the paper is valid for any combination of the dimensional parameters that result in nondimensional parameters within the previously stated ranges; that is, it is no longer necessary to restrict the dimensional parameters to their previously described ranges as long as the nondimensional parameters are restricted to their respective ranges. For example, the analysis is valid for a value of T_0 less than 50 mN or greater than 200 mN as long as the values of $\tilde{m}$, Ω, and L_f are such that $\tilde{T}_0$ falls in the range [0.1, 220]. The following nondimensional analysis is insensitive to different combinations of dimensional parameters that yield the same set of nondimensional parameters.

To investigate the deployment behavior of tethered satellite systems in terms of nondimensional parameters over the relatively wide operating range of the nondimensional parameters, the equations of motion are simulated and analyzed for 30 values of $\tilde{T}_0$ and 30 values of $\tilde{L}'_0$. The nondimensional equations of motion [Eqs. (4–6)] are therefore simulated over the usual range of IPs for 900 different combinations of $\tilde{T}_0$ and $\tilde{L}'_0$. We tabulate the AD and PFD for each combination of nondimensional parameters over the usual range of IPs and show the results in Figs. 12 and 13, respectively. Each entry in the grid corresponds to a different combination of $(\tilde{L}'_0, \tilde{T}_0)$ and is assigned a shade of gray, which indicates the level of either AD or PFD reached at each combination of nondimensional variables. The allocations of the shade are shown in the shade bar on the right side of the grid. Note that the shade bars for AD and PFD grids are similar but not identical. This is to highlight the differences between important levels of PFD and AD. For example, 0% PFD indicates that none of the IPs result in full deployment for a given combination of nondimensional parameters; it is important to know when this happens and hence a shade is dedicated only for that phenomena. On the other hand, 0% AD indicates that none of the IPs deploy at all, which is very unlikely. So a shade is assigned for a low range of AD (rather than just for 0%). However, because 100% AD and 100% PFD represent the same phenomenon (all the IPs deploying completely), the white region is identical in both of the grids.

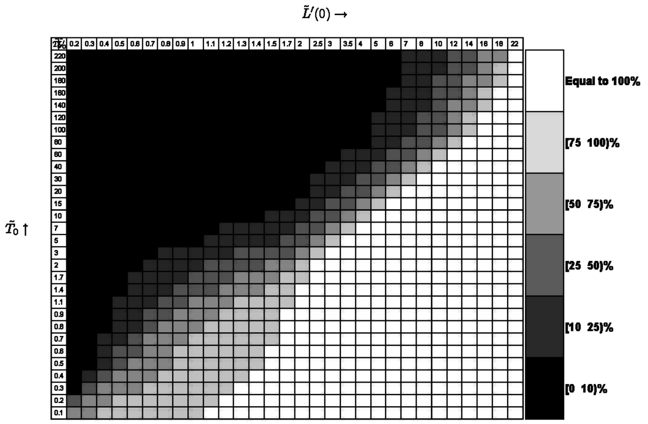

Fig. 12 AD grid for selected $(\tilde{L}'_0, \tilde{T}_0)$ values.

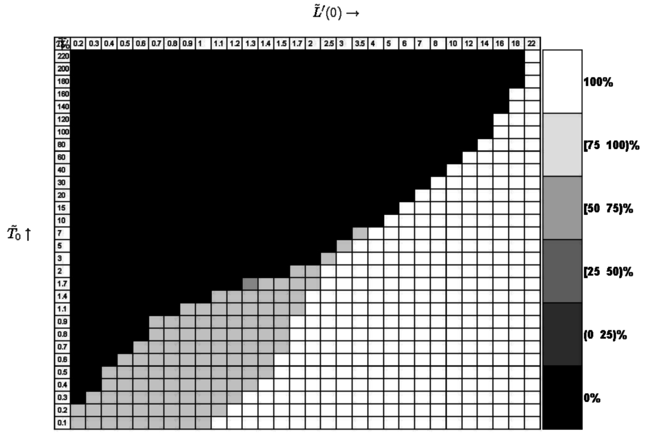

Fig. 13 PFD grid for selected $(\tilde{L}'_0, \tilde{T}_0)$ values.

Now we analyze the deployment behavior in terms of the nondimensional parameters in the context of these grids. From the AD grid in Fig. 12, we can see that the AD increases both with increases in $\tilde{L}'_0$ and decreases in $\tilde{T}_0$. Because $\tilde{L}'_0$ depends on the initial separation velocity $\dot{L}_0$ and $\tilde{T}_0$ depends on the tether friction T_0, the preceding analysis is consistent with the analysis performed using dimensional parameters. We see that at $\tilde{L}'_0 = 22$, complete deployment for all the IPs is achieved, that is, AD = 100% for all the values of $\tilde{T}_0$. Because the level of deployment reached increases with increases in $\tilde{L}'_0$ and the level of deployment over the range of IPs cannot produce an AD higher than 100%, we can assume that the level of deployment will be 100% for all simulations in which $\tilde{L}'_0 > 22$, regardless of the value of $\tilde{T}_0$. Therefore, there is no need to perform simulations for values of $\tilde{L}'_0$ above 22. Note that in Fig. 12, the transition between high and low levels of AD generally occurs diagonally throughout the grid starting from the bottom left corner and ending at the top right corner. The top left triangle of the grid is mostly black, which represents low levels of deployment; the bottom right triangle is mostly white, which represents full deployment. This is consistent with the intuitive assertion that deployment favors low $\tilde{T}_0$ and high $\tilde{L}'_0$.

For any given point along the transition region shown on Fig. 12, increasing $\tilde{L}'_0$ results in an increase in AD; however, increasing $\tilde{T}_0$ results in a decrease in AD. These tendencies create the diagonal nature of the transition region. The same diagonal nature is seen in Fig. 13 with the exception that the transition seems to deviate from a diagonal in the upper right of the figure. To further explore the nature of the transition region, the data represented by Figs. 12 and 13 were plotted on logarithmic scales in Figs. 14 and 15. We have selected 101 points each on the $\tilde{L}'_0$ and $\tilde{T}_0$ scales, thus $101 \times 101 = 10{,}201$

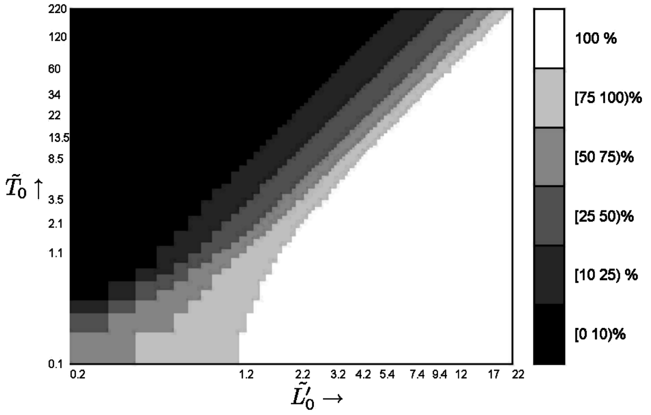

Fig. 14 AD log plot for various values of $(\tilde{L}'_0, \tilde{T}_0)$.

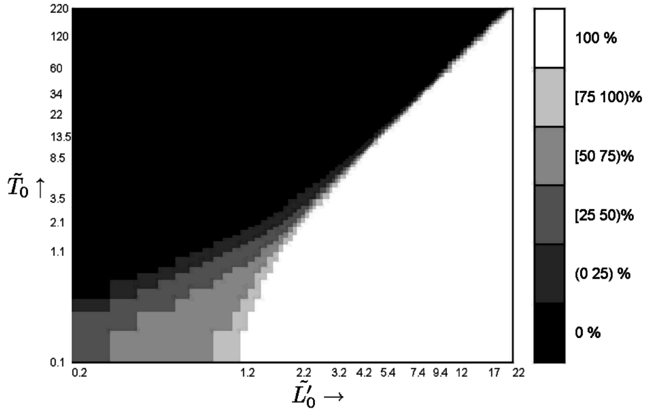

Fig. 15 PFD log plot for various values of $(\tilde{L}'_0, \tilde{T}_0)$.

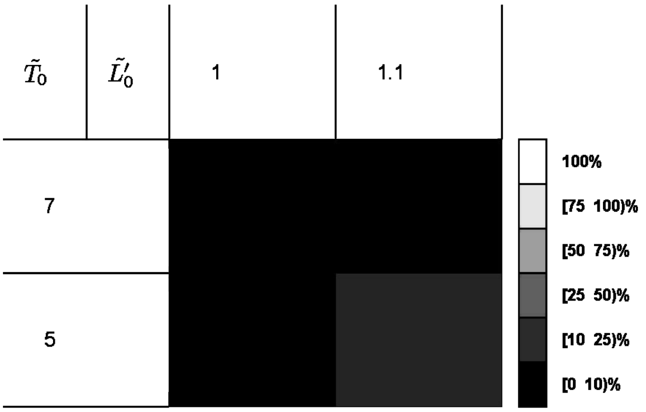

Fig. 16 Zoom in on AD grid for $(\tilde{L}'_0 = 1.01, \tilde{T}_0 = 5.02)$.

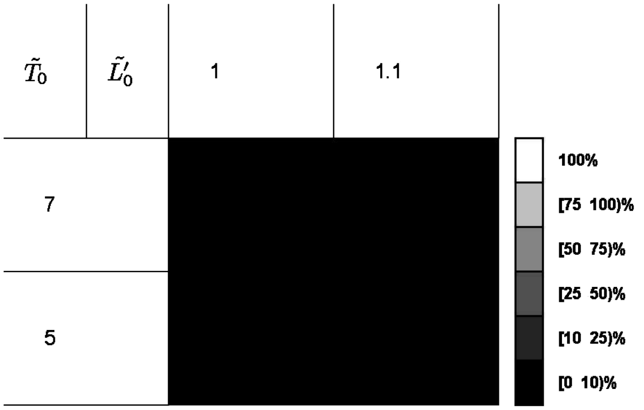

Fig. 17 Zoom in on PFD grid for $(\tilde{L}'_0 = 1.01, \tilde{T}_0 = 5.02)$.

combinations of nondimensional variables were simulated and the resulting AD and PFD are shown on a log-log scale. In these log plots, the shade scales are identical to those in Figs. 12 and 13, but the grid lines are removed for clarity. More detail can be seen in Figs. 14 and 15 than in Figs. 12 and 13, especially in the transition region. Also, because we have used an exponential scale, any point in the operating range of $\tilde{L}'_0$ and $\tilde{T}_0$ can be located on these plots and the corresponding AD and PFD can be estimated. A case study featuring the use of these plots as a design tool will be described in the next section.

VI. Applications

We now demonstrate two applications of the methods previously described. These two applications illustrate how the principles discussed in this paper can be used in two different ways to determine the best set of parameters for optimum tethered satellite system deployment. For convenience, the two nondimensional parameters are written in coordinate form when they appear together to represent the entire system configuration. For example, $\tilde{L}'_0 = 2$ and $\tilde{T}_0 = 3$ are written as $(\tilde{L}'_0 = 2, \tilde{T}_0 = 3)$.

A. Mission Design from Given Parameters

We will show how the tools previously developed can be used to adjust tethered satellite mission parameters to achieve full tethered satellite deployment. Such an analysis could be performed midway through the mission design process to determine adjustments that need to be made to tethered satellite parameter values to achieve full deployment. To estimate the amount of deployment that will take place with the given parameters, we calculate the values of $\tilde{L}'_0$ and $\tilde{T}_0$ and use Figs. 14 and 15 to estimate the expected level of average deployment and the percentage of IPs reaching full deployment. Based on the location of the point $(\tilde{L}'_0, \tilde{T}_0)$ relative to the transition region, we determine the most appropriate change in the design parameters that will result in full tethered satellite deployment. Let us assume a 70 kg tethered satellite mission similar to the TAG mission previously discussed with mission parameters [$h = 1000$ km, $L_f = 2.4$ km]. Let us also assume that the two halves of the tethered satellite separate at a velocity of 3 m/s and that the internal deployment mechanism friction (and thus the tether tension) is 185 mN. We also assume that the end-body masses are distributed so that the effective mass is 10 kg. The design parameters corresponding to this physical configuration are [$T_0 = 185$ mN, $\bar{m} = 10$ kg, $\dot{L}_0 = 3$ m/s]. From Eq. (7) this configuration gives the nondimensional variable values $(\tilde{L}'_0 = 1.01, \tilde{T}_0 = 5.02)$. It would be difficult to estimate the AD for such a configuration using only Fig. 12 because the spacing between the grid points of Fig. 12 is too large. We can narrow down our region of interest by zooming in on a subgrid around the point of interest as shown in Fig. 16

We see that this subgrid has only bottom two shades of the shade bar, together indicating [0, 25)% of deployment at the point of interest. Now we examine the same subgrid on a plot showing PFD as a function of $\tilde{L}'_0$ and $\tilde{T}_0$; this subgrid is shown in Fig. 17. The entire grid is black and hence we can be certain that, at this point of interest, the PFD is 0%.

We can see that the AD is below 25% and the PFD is 0%. To achieve better performance, we need to move diagonally down the grid and toward the right. This can be done by increasing $\tilde{L}'_0$ and decreasing $\tilde{T}_0$. To increase $\tilde{L}'_0$, let us assume that the separation mechanism employs a stiff spring resulting in the highest considered initial separation velocity: 6 m/s. The new configuration yields $(\tilde{L}'_0 = 2.02, \tilde{T}_0 = 5.02)$, which moves the point of interest toward the right of the grid. Now to move down the grid, we lower the value of $\tilde{T}_0$. We accomplish this by increasing the effective mass through equal redistribution of the end-body masses, giving the maximum value of $\bar{m}$, as calculated earlier to be 17.5 kg. The nondimensional parameters are now $(\tilde{L}'_0 = 2.02, \tilde{T}_0 = 2.87)$. With these two steps,

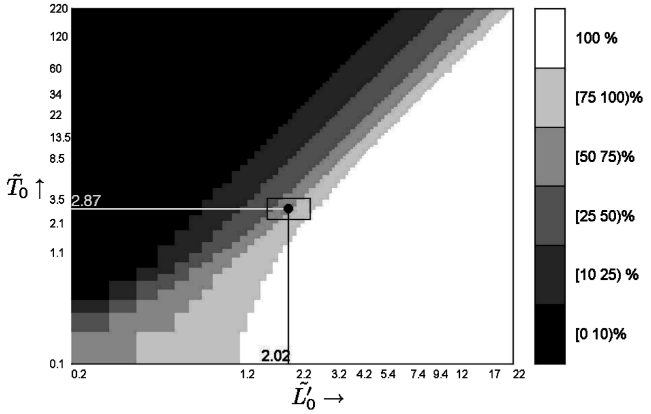

Fig. 18 **AD log plot for ($\tilde{L}'_0 = 2.02$, $\tilde{T}_0 = 2.87$).**

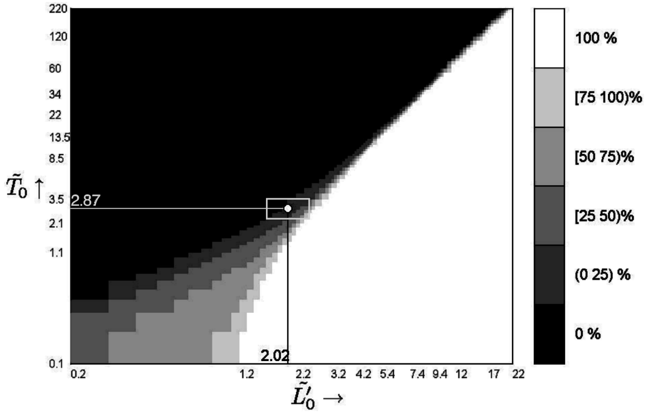

Fig. 19 **PFD log plot for ($\tilde{L}'_0 = 2.02$, $\tilde{T}_0 = 2.87$).**

we effectively moved the point of interest diagonally down the grid toward the right. Now instead of using the grid plots, we zoom in on the more refined tool, that is, the log plots. We can locate the point ($\tilde{L}'_0 = 2.02, \tilde{T}_0 = 2.87$) on the both the plots as shown in Figs. 18 and 19. We notice that this configuration is located on the point representing an AD in [50, 75)% range and PFD in the (0, 25)% range. This can be verified by the deployment vs IP curves shown in Fig. 20. The AD is still not at its maximum value, even at optimum values for $\bar{m}$ and $\dot{L}_0$. We now attempt to raise the AD by assuming a reduction in T_0, that is, by reducing $\tilde{T}_0$ and hence, moving further down the AD grid. Assume a decrease in T_0 (i.e., a decrease in the internal friction of the deployment mechanism) to 90 mN. The nondimensional design parameters of this configuration are ($\tilde{L}'_0 = 2.02$, $\tilde{T}_0 = 1.40$). From the initial grids (Figs. 12 and 13) it is clear that for this configuration, AD and PFD are 100%. The deployment curves for this configuration can be seen in Fig. 21. This application demonstrates how the PFD and AD grids can be used to determine changes necessary to a tethered satellite physical configuration to achieve an AD of 100%.

B. Mission Parameter Determination

We will now demonstrate how mission parameters can be actively selected (rather than adjusted) to obtain the desired deployment behavior. This differs from the previous design method in that we will demonstrate how mission parameters can be selected to achieve full deployment with a limited amount of knowledge about the system rather than demonstrating how mission parameters can be adjusted to achieve full tethered satellite deployment. Assume that the given design criteria call for a 70 kg tethered satellite mission operating at an orbital height $h = 1200$ km with a final deployed tether length $L_f = 3$ km. We now attempt to determine a set of parameters that will result in full deployment. From the given information, and the definition of $\tilde{T}_0$ and $\tilde{L}'_0$ as given in Eq. (7), we can immediately calculate

$$\tilde{T}_0 = \frac{T_0/\bar{m}}{0.0027482} \quad \text{and} \quad \tilde{L}'_0 = \frac{\dot{L}(0)}{2.8714} \tag{8}$$

From the operating range of dimensional parameters, discussed earlier in the paper, we can also calculate the range of $T_0/\bar{m}$ as [0.0028571 mN/kg, 0.02 mN/kg] and we know that range of $\dot{L}_0$ is [3 m/s, 6 m/s]. From this we can compute the range of nondimensional parameters as $\tilde{T}_0$ as [1.039, 7.27] and that of $\tilde{L}'_0$ as [1.048, 2.0896].

Now, with the minimum and maximum value of both the nondimensional parameters, we can narrow the AD grid as shown in Fig. 22. The final parameters selected for the tethered satellite system must give nondimensional parameter values that lie in the subgrid described by Fig. 22. In this subgrid, only two points give 100% PFD and AD, ($\tilde{L}'_0 = 2$, $\tilde{T}_0 = 1.1$) and ($\tilde{L}'_0 = 2$, $\tilde{T}_0 = 1.4$). It is generally difficult to reduce the T_0 because of its dependence on the internal friction of the deployment mechanism; therefore, we choose a point that allows for higher T_0, that is, higher $\tilde{T}_0$. We choose the point ($\tilde{L}'_0 = 2$, $\tilde{T}_0 = 1.4$) as nondimensional parameters and choose dimensional parameters that correspond to these nondimensional parameters. Substituting the nondimensional parameters into Eqs. (8), we have $\dot{L}_0 = 5.75$ m/s and $T_0/\bar{m} = 0.0038$ mN/kg. If we equally distribute the mass, that is, set $\bar{m} = 17.5$ kg, then $T_0 = 67.3$ mN. In summary, the dimensional design parameters for this system are [$T_0 = 67.3$ mN, $\bar{m} = 17.5$ kg, $\dot{L}_0 = 5.75$ m/s] and the mission parameters are [$h = 1200$ km, $L_f = 3$ km] and the

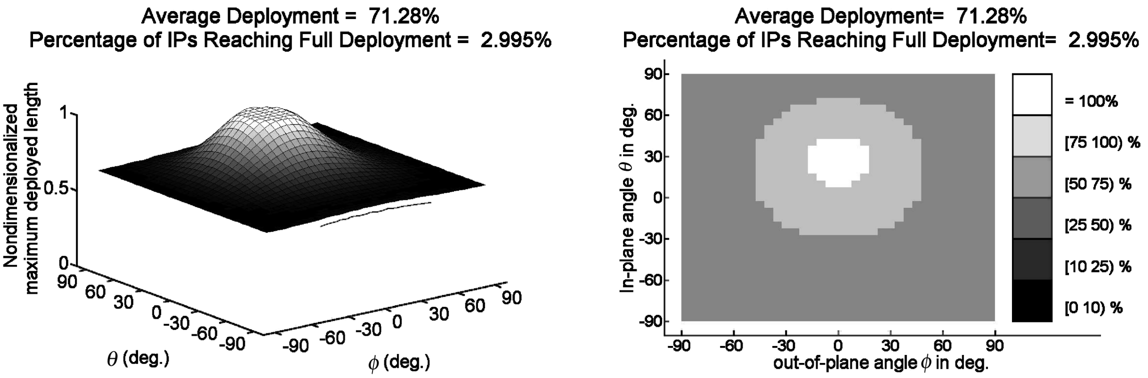
Average Deployment = 71.28%
Percentage of IPs Reaching Full Deployment = 2.995%

Average Deployment= 71.28%
Percentage of IPs Reaching Full Deployment= 2.995%

a) 3-D representation with IPs on horizontal plane and deployed length on vertical axis

b) 2-D representation with ϕ on horizontal axis and θ on vertical axis

Fig. 20 **Deployment curves for ($\tilde{L}'_0 = 2.02$, $\tilde{T}_0 = 2.87$).**

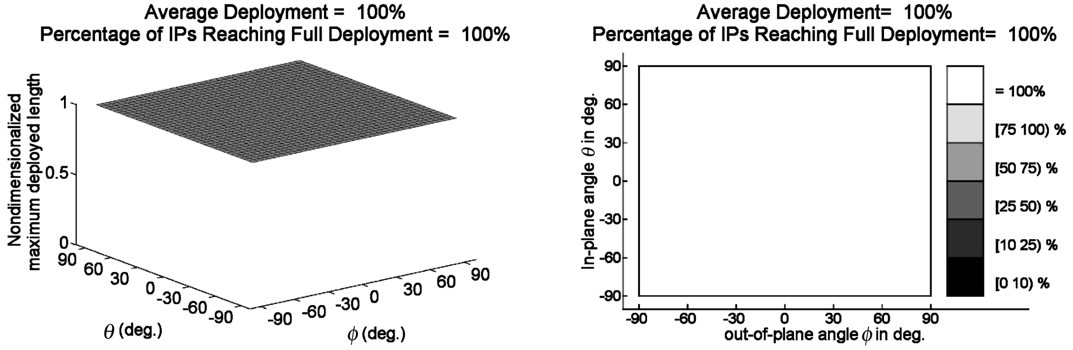

a) 3-D representation with IPs on horizontal plane and deployed length on vertical axis

b) 2-D representation with ϕ on horizontal axis and θ on vertical axis

Fig. 21 Deployment curves for ($\tilde{L}_0' = 1.4$, $\tilde{T}_0 = 2.02$).

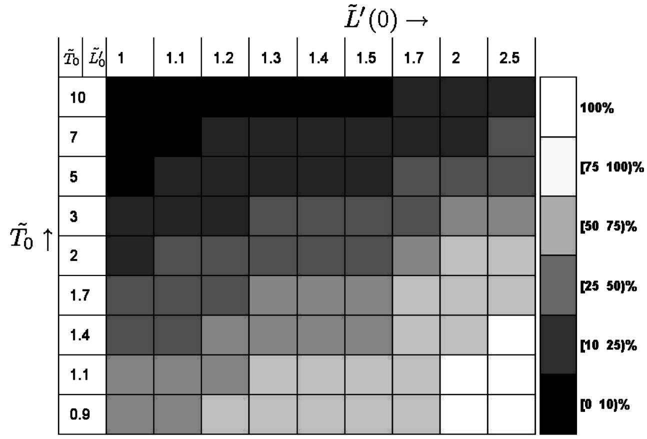

Fig. 22 AD subgrid for parameter identification. $\tilde{L}_0'$ arranged by columns and $\tilde{T}_0$ arranged by rows.

tethered satellite system exhibiting these parameters will deploy fully for all initial angular displacements.

VII. Conclusions

This paper presents a detailed study of the factors affecting the deployment dynamics of a tethered satellite system. Five dimensional parameters that affect the percentage of the total length to which a tether deploys are identified. These parameters include the initial separation velocity, the tether tension force, the orbital height, the effective mass (which measures the distribution of the tethered satellite end-body masses), and the final desired tether length. Through numerical simulations, we determined that the final length a tethered satellite reaches under uncontrolled deployment increases with increasing initial separation velocity, increasing effective mass, and decreasing tether tension (which is equal to deployer friction). Furthermore, we note that the final deployment length increases as the angle between the tether and the orbital plane approaches zero; that is, the final deployment length is larger if the tether deployment begins in the orbital plane than if the tether deployment begins outside of the orbital plane. We also note that the maximum final tether length with respect to in-plane initial angle occurs at a point close to, but not equal to, an in-plane angle of zero. By nondimensionalizing the equations of motion, we define two nondimensional variables that completely describe the tether deployment dynamics. By numerically integrating the nondimensional equations of motion, we show that the final tether deployment length increases with decreasing nondimensional tension and increases with increasing nondimensional initial velocity. We also show the utility of the nondimensional parameters from a mission design standpoint and provide case studies that demonstrate the use of the nondimensional parameters as tools useful in determining the final deployment length of a tethered satellite without solving the equations of motion.

Appendix: Derivation of the Tethered Satellite Equations of Motion

The equations of motion for a tethered satellite consisting of two point masses in a circular orbit are derived as follows. Note that all quantities are defined in Fig. 2.

We begin by writing Newton's Second Law in the form

$$\frac{\boldsymbol{F}_A}{m_A} - \frac{\boldsymbol{F}_B}{m_B} = \boldsymbol{a}_{A/E} - \boldsymbol{a}_{B/E} = \boldsymbol{a}_{A/B} \tag{A1}$$

1. Forces

We assume that each end body is only acted upon by a gravitational force and tether tension force. Hence the left-hand side of Eq. (A1) is expressed

$$\begin{aligned}\frac{\boldsymbol{F}_A}{m_A} - \frac{\boldsymbol{F}_B}{m_B} &= \left(\frac{-GM_e}{|\boldsymbol{r}_{A/E}|^2}\frac{\boldsymbol{r}_{A/E}}{|\boldsymbol{r}_{A/E}|} + \frac{T}{m_A}\frac{\boldsymbol{r}_{C/A}}{|\boldsymbol{r}_{C/A}|}\right)\\ &\quad - \left(\frac{-GM_e}{|\boldsymbol{r}_{B/E}|^2}\frac{\boldsymbol{r}_{B/E}}{|\boldsymbol{r}_{B/E}|} + \frac{T}{m_B}\frac{\boldsymbol{r}_{C/B}}{|\boldsymbol{r}_{C/B}|}\right)\\ \Rightarrow \frac{\boldsymbol{F}_A}{m_A} - \frac{\boldsymbol{F}_B}{m_B} &= \left(\frac{-GM_e}{|\boldsymbol{r}_{A/E}|^3}\boldsymbol{r}_{A/E} + \frac{T}{m_A}\frac{\boldsymbol{r}_{C/A}}{|\boldsymbol{r}_{C/A}|}\right)\\ &\quad - \left(\frac{-GM_e}{|\boldsymbol{r}_{B/E}|^3}\boldsymbol{r}_{B/E} + \frac{T}{m_B}\frac{\boldsymbol{r}_{B/E}}{|\boldsymbol{r}_{B/E}|}\right)\end{aligned} \tag{A2}$$

Note that

$$\frac{\boldsymbol{r}_{C/A}}{|\boldsymbol{r}_{C/A}|} = \begin{bmatrix} -1 \\ 0 \\ 0 \end{bmatrix} \quad \text{and} \quad \frac{\boldsymbol{r}_{C/B}}{|\boldsymbol{r}_{C/B}|} = \begin{bmatrix} -1 \\ 0 \\ 0 \end{bmatrix}$$

Also note that vectors $\boldsymbol{r}_{A/E}$ and $\boldsymbol{r}_{B/E}$ can be expressed in the satellite reference frame as

$$\{\boldsymbol{r}_{A/E}\}_S = \{\boldsymbol{r}_{A/C}\}_S + \{\boldsymbol{r}_{C/E}\}_S = \begin{bmatrix} L_a + R\cos\theta\cos\phi \\ -R\sin\theta \\ -R\cos\theta\sin\phi \end{bmatrix}$$

$$\Rightarrow |\boldsymbol{r}_{A/E}| = (R^2 + L_a^2 + 2RL_a\cos\theta\cos\phi)^{\frac{1}{2}}$$

$$= R\left(1 + \frac{L_a^2}{R^2} + \frac{2L_a}{R}\cos\theta\cos\phi\right)^{\frac{1}{2}}$$

If the total tether length is small compared to the orbital radius, the term L_a^2/R^2 is negligible compared to 1 and can be assumed to be approximately equal to zero. Further, using the binomial expansion to compute the reciprocal of the cube of the magnitude, we can write

$$|\boldsymbol{r}_{A/E}|^{-3} \approx \frac{1}{R^3}\left(1 - 3\frac{L_a}{R}\cos\theta\cos\phi\right)$$

Similarly,

$$\{\boldsymbol{r}_{B/E}\}_S = \begin{bmatrix} -L_b + R\cos\theta\cos\phi \\ -R\sin\theta \\ -R\cos\theta\sin\phi \end{bmatrix},$$

$$|\boldsymbol{r}_{B/E}|^{-3} \approx \frac{1}{R^3}\left(1 + 3\frac{L_b}{R}\cos\theta\cos\phi\right)$$

Using the definition $GM_e/R^3 = \Omega^2$, substituting in Eq. (A2), and simplifying, yields

$$\left\{\frac{\boldsymbol{F}_A}{m_A} - \frac{\boldsymbol{F}_B}{m_B}\right\}_S = \begin{bmatrix} -\Omega^2 L + 3\Omega^2 L\cos^2\theta\cos^2\phi - \frac{T}{\bar{m}} \\ -3\Omega^2 L\cos\theta\sin\theta\cos\phi \\ -3\Omega^2 L\cos^2\theta\cos\phi\sin\phi \end{bmatrix} \tag{A3}$$

2. Acceleration

The relative angular velocity and angular acceleration between the inertial E frame and satellite S frame can be expressed as (note that the angular acceleration is obtained by differentiating the angular velocity)

$${}^E\boldsymbol{\omega}^S = \begin{bmatrix} (\dot\theta + \Omega)\sin\phi \\ -\dot\phi \\ (\dot\theta + \Omega)\cos\phi \end{bmatrix},$$

$${}^E\boldsymbol{\alpha}^S = \begin{bmatrix} \ddot\theta\cos\phi + (\dot\theta + \Omega)\dot\phi\cos\phi \\ -\ddot\phi \\ \ddot\theta\cos\phi - (\dot\theta + \Omega)\dot\phi\sin\phi \end{bmatrix}$$

Note that

$$\{\boldsymbol{r}_{A/B}\}_S = \begin{bmatrix} L \\ 0 \\ 0 \end{bmatrix}, \qquad \{{}^S\dot{\boldsymbol{r}}_{A/B}\}_S = \begin{bmatrix} \dot L \\ 0 \\ 0 \end{bmatrix}, \qquad \{{}^S\ddot{\boldsymbol{r}}_{A/B}\}_S = \begin{bmatrix} \ddot L \\ 0 \\ 0 \end{bmatrix}$$

The inertial acceleration, that is, derivative of the velocity in the E frame can be found using the relation

$$\begin{aligned} {}^E\ddot{\boldsymbol{r}}_{A/B} &= {}^S\ddot{\boldsymbol{r}}_{A/B} + {}^E\boldsymbol{\alpha}^S \times \boldsymbol{r}_{A/B} + 2{}^E\boldsymbol{\omega}^S \times {}^S\dot{\boldsymbol{r}}_{A/B} \\ &\quad + {}^E\boldsymbol{\omega}^S \times ({}^E\boldsymbol{\omega}^S \times \boldsymbol{r}_{A/B}) \end{aligned} \tag{A4}$$

Substituting all the variables with expressions we computed, and simplifying, we obtain

$$\{{}^E\ddot{\boldsymbol{r}}_{A/B}\}_S = \begin{bmatrix} \ddot L - \dot\phi^2 L - (\dot\theta + \Omega)^2\cos^2\phi L \\ \ddot\theta\cos\phi L - 2(\dot\theta + \Omega)\dot\phi\sin\phi + 2(\dot\theta + \Omega)\dot L\cos\phi \\ \ddot\phi L + 2\ddot\phi\dot L + (\dot\theta + \Omega)^2\cos\phi\sin\phi L \end{bmatrix} \tag{A5}$$

Using Eq. (A1), Eqs. (A3) and (A5) can be set equal to each other to obtain

$$\begin{bmatrix} \ddot L - \dot\phi^2 L - (\dot\theta + \Omega)^2\cos^2\phi L \\ \ddot\theta\cos\phi L - 2(\dot\theta + \Omega)\dot\phi\sin\phi + 2(\dot\theta + \Omega)\dot L\cos\phi \\ \ddot\phi L + 2\ddot\phi\dot L + (\dot\theta + \Omega)^2\cos\phi\sin\phi L \end{bmatrix}$$

$$= \begin{bmatrix} -\Omega^2 L + 3\Omega^2 L\cos^2\theta\cos^2\phi - \frac{T}{\bar{m}} \\ -3\Omega^2 L\cos\theta\sin\theta\cos\phi \\ -3\Omega^2 L\cos^2\theta\cos\phi\sin\phi \end{bmatrix}$$

The final differential equations of motion are then

$$\ddot L = L[(\dot\theta + \Omega)^2\cos^2\phi + \dot\phi^2 + 3\Omega^2\cos^2\theta\cos^2\phi - \Omega^2] - \frac{T}{\bar{m}} \tag{A6}$$

$$\ddot\theta = 2(\dot\theta + \Omega)\dot\phi\tan\phi - 2\frac{\dot L}{L}(\dot\theta + \Omega) - 3\Omega^2\cos\theta\sin\theta \tag{A7}$$

$$\ddot\phi = -2\frac{\dot L}{L}\dot\phi - [(\dot\theta + \Omega)^2 + 3\Omega^2\cos^2\theta]\cos\phi\sin\phi \tag{A8}$$

References

[1] Beardsley, T., "The Way To Go In Space," *Scientific American*, Vol. 280, No. 2, Feb. 1999, p. 81.

[2] Lorenzini, E., and Sanmartin, J., "Electrodynamic Tethers in Space," *Scientific American*, Vol. 291, No. 2, Aug. 2004, pp. 50–57.

[3] Bray, B., and Jaap, J., "Tethers in Space," *NASA: Liftoff to Space Exploration*, NASA, Jan. 2001.

[4] Iess, L., Bruno, C., Ulivieri, C., and Vannaroni, G., "Satellite De-Orbiting By Means of Electrodynamic Tethers, Part 2: System Configuration and Performance," *Acta Astronautica*, Vol. 50, No. 7, April 2002, pp. 407–416.

[5] Williams, P., "Optimal Orbital Transfer with Electrodynamic Tethers," *Journal of Guidance, Control, and Dynamics*, Vol. 28, No. 2, April 2005, pp. 369–372.

[6] van der Heide, E., and Kruijff, M., "Tethers and Debris Mitigation," *Acta Astronautica*, Vol. 48, Nos. 5–12, 2001, pp. 503–516.

[7] Iess, L., Bruno, C., Ulivieri, C., Ponzi, U., Parisse, M., Laneve, G., Vannaroni, G., Dobrowolny, M., De Venuto, F., Bertotti, B., and Anselmo, L., "Satellite De-orbiting by Means of Electrodynamic Tethers, Part 1: General Concepts and Requirements," *Acta Astronautica*, Vol. 50, No. 7, April 2002, pp. 399–406.

[8] Ishige, Y., Kawamoto, S., and Kibe, S., "Study On Electrodynamic Tether Systems for Space Debris Removal," *Acta Astronautica*, Vol. 55, No. 11, 2004, pp. 917–92.

[9] Williams, P., Blanksby, C., Trivailo, P., and Fujii, H. A., "In-Plane Payload Capture Using Tethers," *Acta Astronautica*, Vol. 57, No. 10, Nov. 2005, pp. 772–787.

[10] Pelaez, J., "On The Dynamics of Deployment of the Tether from an Orbiter—Part 2," *Acta Astronautica*, Vol. 36, No. 6, 1995, pp. 313–335.

[11] Anselmo, L., and Pardini, C., "The Survivability of Space Tether Systems in Orbit Around the Earth," *Acta Astronautica*, Vol. 56, No. 3, 2005, pp. 391–396.

[12] Modi, V., and Misra, A., "On the Deployment Dynamics of Tether Connected Two-Body Systems," *Acta Astronautica*, Vol. 9, No. 9, 1979, pp. 1183–1197.

[13] Edwards, B., "The Space Elevator: Concept Overview," *Proceedings of Space 2002 and Robotics 2002*, American Society of Civil Engineers, Reston, VA, March 2002, pp. 77–83.

[14] Smith, A., "A High Payload Capacity Tether System," *Proceedings of Space 2002 and Robotics 2002*, American Society of Civil Engineers, Reston, VA, March 2002, pp. 91–95.

[15] Edwards, B., "Design and Deployment of a Space Elevator," *Acta Astronautica*, Vol. 47, No. 10, 2000, pp. 735–744.

[16] Person, J., "The Orbital Tower: A Spacecraft Launcher Using the Earth's Rotational Energy," *Acta Astronautica*, Vol. 2, 1975, pp. 785–799.

[17] Mazzoleni, A., and Hoffman, J., "Overview of the TAG (Tethered Artificial Gravity) Satellite Program," *Advances in the Astronautical Sciences*, Vol. 112, No. 2, 2002, pp. 1291–1300.

[18] Lorenzini, E., and Cosmo, M., *Tethers In Space Handbook*, 3rd ed., NASA, Dec. 1997.

[19] Modi, V., and Misra, A., "On the Deployment Dynamics of Tether Connected Two Body Systems," *Acta Astronautica*, Vol. 6, No. 9, Sept. 1979, pp. 1183–1197.

[20] Pascal, M., Djebli, A., and El Bakkali, L., "Laws of Deployment/Retrieval in Tether Connected Satellites Systems," *Acta Astronautica*, Vol. 45, No. 2, 1999, pp. 61–73.

[21] Barkow, B., Steindl, A., and Troger, H., "A Targeting Strategy for the Deployment of a Tethered Satellite System," *IMA Journal of Applied Mathematics*, Vol. 70, No. 5, 2005, pp. 626–644.

[22] Lorenzini, E., Bortolami, S., Rupp, C., and Angrilli, F., "Control and Flight Performance of Tethered Satellite Small Expendable Deployment System-2," *Journal of Guidance, Control, and Dynamics*, Vol. 19, No. 5, 1996, pp. 1148–1156.

[23] Carroll, J., "SEDS Deployer Design and Flight Performance," AIAA Paper 1993-4764, Sept. 1993.

[24] Grassi, M., and Cosmo, M., "Attitude Dynamics of the Small Expendable-Tether Deployment System," *Acta Astronautica*, Vol. 36, No. 3, Aug. 1995, pp. 141–148.

[25] Mazzoleni, A., "Nonplanar Deployment Dynamics of the Astor Tethered Satellite System," *AAS/AIAA Space Flight Mechanics Meeting*, Univelt, San Diego, CA, Jan. 2000, pp. 1307–1326.

[26] Bainum, P., and Kumar, V., "Optimal Control of the Shuttle-Tethered-Subsatellite System," *Acta Astronautica*, Vol. 7, No. 12, 1980, pp. 133–1348.

[27] Biswell, B., and Puig-Suari, J., "Lifting Body Effects on the Equilibrium Orientation of Tethers in the Atmosphere," *Acta Astronautica*, Vol. 43, No. 9, 1998, pp. 521–529.

[28] Mazzoleni, A. P., "Nonplanar Deployment Dynamics of the ASTOR Tethered Satellite System," *Advances in the Astronautical Sciences*, Vol. 105, No. 2, 2000, pp. 1307–1317.

[29] Bilen, S., "Space-Born Tethers," *IEEE Potentials*, Vol. 13, No. 3, Aug. 1994, pp. 47–50.

[30] Arnold, D., "The Behavior of Long Tethers in Space," *Journal of the Astronautical Sciences*, Vol. 35, No. 1, 1987, pp. 3–18.

C. McLaughlin
Associate Editor